

Effects of ram pressure on the gas distribution and star formation in the Large Magellanic Cloud.

Chiara Mastropietro ¹ \star , Andreas Burkert ², Ben Moore ³

¹ *LERMA, Observatoire de Paris, UPMC, CNRS, 61 Av. de l'Observatoire, 75014 Paris, France*

² *Universitäts Sternwarte München, Scheinerstr.1, D-81679 München, Germany*

³ *Institute for Theoretical Physics, University of Zürich, CH-8057 Zürich, Switzerland*

29 October 2018

ABSTRACT

We use high resolution N-body/SPH simulations to study the hydrodynamical interaction between the Large Magellanic Cloud (LMC) and the hot halo of the Milky Way. We investigate whether ram-pressure acting on the satellite's ISM can explain the peculiarities observed in the HI distribution and the location of the recent star formation activity.

Due to the present nearly edge-on orientation of the disk with respect to the orbital motion, compression at the leading edge can explain the high density region observed in HI at the south-east border. In the case of a face-on disk (according to Mastropietro et al. 2008 the LMC was moving almost face-on before the last perigalactic passage), ram-pressure directed perpendicularly to the disk produces a clumpy structure characterized by voids and high density filaments that resemble those observed by the Parkes HI survey. As a consequence of the very recent edge-on motion, the H α emission is mainly concentrated on the eastern side where 30 Doradus and most of the supergiant shells are located, although some H α complexes form a patchy distribution on the entire disk. In this scenario only the youngest stellar complexes show a progression in age along the leading border of the disk.

Key words: methods: N-body simulations – hydrodynamics – galaxies: interactions – galaxies: individual: LMC

1 INTRODUCTION

The Large Magellanic Cloud (LMC) has revealed a very complex structure both in the stellar and in the gaseous component. The elongation of the stellar disk in the direction of the Galactic center, its substantial vertical thickness, the warp and the strong asymmetric bar are naturally predicted by numerical simulations as a result of the gravitational interaction between the LMC and the Galaxy (Bekki & Chiba 2005, Mastropietro et al. 2005, hereafter M05). The old stellar distribution appears to be quite smooth in the outer parts of the disk, with no signs of spiral structures out to a radius of 10 kpc (van der Marel 2001). Within the same radius the HI large scale structure reveals the presence of several asymmetric features that have no equivalent in the old stellar disk. The gaseous disk is characterized by the presence of an elongated region located at the south-east of the galaxy and aligned with the border of the optical disk, where the column density distribution shows a steep increase (Staveley-Smith et al. 2003; Putman et al. 2003).

Since the LMC proper motion vector is directed to the east, it appears natural to associate this high density region with ram-pressure acting on the leading edge of the disk due to the orbital motion of the LMC and its consequent interaction with the diffuse hot gas in the halo of the Milky Way (MW).

The presence of an extended hot halo surrounding galaxies and in hydrostatic equilibrium within the dark matter potential is expected by current models of hierarchical structure formation (Maller & Bullock 2004). In the MW, X-ray absorption lines produced by hot ($T \sim 10^6$ K) gas are detected in the spectra of several bright AGN (Williams et al. 2005; Fang et al. 2006). Some ionization features discovered in the Magellanic Stream and high velocity Clouds indicate that this distribution of hot gas extends well beyond the Galactic disk (> 70 kpc). Constraints from dynamical and thermal arguments fix its density in a range between 10^{-5} and 10^{-4} cm $^{-3}$ at the LMC distance from the Galactic center (but Kaufmann et al. 2009 suggest a value ten times higher).

Cioni et al. (2006) have performed a detailed analysis of the LMC global star formation rate using asymptotic giant

\star E-mail: chiara.mastropietro@obspm.fr

branch stars. They find an irregular and patchy distribution in age, with the youngest carbon-rich systems located at the south-east of the disk. The present star formation activity is rather clumpy and concentrated in stellar complexes characterized by intense HII emission and associated with bright H α filamentary bubbles. Most of these very young structures lie on the south-east of the disk, in the proximity of 30 Doradus, the largest star forming region of the LMC, some are located in the bar and the remainder form an asymmetric pattern that covers the entire disk with no apparent relation to the global geometry of the satellite.

It is not clear which is the overall physical mechanism responsible for triggering star formation with the observed asymmetric pattern and different models have been proposed in the past. The stochastic self-propagating star formation (SSPSF) model (Gerola & Seiden 1978) predicts a clear age gradient in the LMC’s stellar complexes, with the edges being younger with respect to the center, in contradiction with observations (Braun et al. 1997). de Boer et al. (1998) proposed a scenario where the bow shock originated by the motion of the LMC through the hot galactic halo compresses the leading edge of the disk and induces star formation. The pressure at the south-eastern edge of the LMC is indeed 10 times higher than the average in the rest of the LMC (Blondiau et al. 1997). This model, which assumes the orbital motion vector lying in the plane of the disk, predicts increasing ages of the stellar complexes in the direction of the rotation, due to the fact that the material compressed at the front side of the disk moves, in time, away to the side. The youngest systems would indeed lie at the south-east border of the disk, where the relative velocity between the corotating interstellar medium and the external diffuse gas is maximum. Several giant structures along the outer east and north edge of the LMC actually show a progression in age in a clockwise direction: moving from south-east to the north LMC 2, 30 Doradus and LMC 3, LMC 4, NGC1818. In particular the difference in age between 30 Doradus and LMC4 is exactly their distance along the border of the disk divided by the satellite’s rotational velocity (Harris, private communication). Grebel & Brandner (1998) studied the recent star formation history of the LMC using Cepheids and other supergiant stars and found that although the majority of the star formation events in the last 30 Myr are concentrated on the east border, others are distributed across the entire disk in partial contrast with the bow shock induced star formation model, that can not explain them.

In this work we use high resolution SPH simulations to study the effects of the interaction between the LMC interstellar medium and the diffuse hot halo of the MW. We want to investigate whether the ram-pressure acting on the leading edge of the LMC disk is responsible for the increase in density observed in the south-east and for triggering star formation. The analytic model of de Boer et al. (1998) assumes a pure edge-on model, but according to van der Marel et al. (2002) the present angle between the LMC disk and the orbital motion is nearly 30°. Even in the absence of precession and nutation, this angle is subjected to large variations during the orbital period in such a way that compression produced by the external hot gas can affect in time both edge-on and face-on.

Moreover, the ram-pressure felt by the LMC is not constant and has a maximum when the satellite approaches the

perigalacticon. The motion of the LMC through the hot halo of the MW during the last 1 Gyr is modeled using “test wind tunnel” simulations with increasing ram-pressure values.

The paper is structured as follows. Section 2 describes the models and the star formation criteria adopted, Section 3 illustrates the results of simulations without star formation, focussed on the investigation of pure effects of compression on the LMC interstellar medium while Section 4 describes the runs where star formation is activated. Several simulations have been performed, assuming different star formation models, disk inclinations and hot halo densities.

2 SIMULATIONS

2.1 Galaxy model

The initial conditions of the simulations are constructed using the technique described by Hernquist (1993). Our disk galaxy model is a multi-component system with a stellar and gaseous disk embedded in a spherical NFW (Navarro, Frenk & White 1997) dark matter halo. The density profile of the dark matter halo is adiabatically contracted in response to baryonic infall (Blumenthal et al. 1986). The stellar disk follows an exponential surface density profile of the form:

$$\Sigma(R) = \frac{M_d}{2\pi R_d^2} \exp(-R/R_d), \quad (1)$$

where M_d and R_d are the disk mass and radial scale length (in cylindrical coordinates), respectively, while the thin vertical structure has a scale length $z_d \sim \frac{1}{5} R_d$:

$$\rho_d(R, z) = \frac{\Sigma(R)}{2z_d} \operatorname{sech}^2(z/z_d). \quad (2)$$

The gaseous disk is characterized by an exponential profile with the same radial and vertical scale length as the stellar component and by a constant density layer which extends up to $8R_d$.

The structural parameters of the disk and the halo are chosen so that the resulting rotation curve resembles that of a typical bulgeless late-type (Sc/Sd) disk galaxy (Courteau 1997; Persic & Salucci 1997). They are similar to those adopted in M05 for the initial LMC model and reproduce quite well the peak of the rotation curve inferred by van der Marel et al. (2002) (Fig. 1). As seen in M05, the interaction with the MW does not affect significantly the stellar and dark matter mass in the inner 8 – 9 kpc of the LMC and consequently the global rotation curve within this radial range. The choice of an extended gaseous component for the initial LMC model is motivated by the fact that spiral galaxies in the local universe are commonly observed to be embedded in extended disks of neutral hydrogen significantly larger than their stellar component (Hunter & Gallagher 1985; Broeils & van Woerden 1994). As seen in M05, the combined effect of tidal interactions and ram-pressure stripping can remove a significant fraction of gas from a LMC disk orbiting within the hot halo of the MW, with a ram-pressure stripping radius which is a factor of three smaller than the initial radius of the gaseous disk. Also in the case of a LMC with orbital velocities significantly higher (Mastropietro 2008) hydrodynamic and gravitational forces together are effective in resizing and reshaping the extended

gaseous disk of the satellite beyond 8 kpc. In the present work we neglect the presence of gravitational forces focusing on the effects of pure ram-pressure. Therefore we do not expect to see a significant decrease in the radius of the gas distribution. However, in order to take in account the loss of cold gas from the disk of the satellite and the star formation events, we assumed an initial amount of gas in the disk which is about 3 times larger than the HI mass in the LMC ($2.9 \times 10^8 M_\odot$ according to Putman et al. 2003).

The mass within the virial radius is set equal to $2.18 \times 10^{10} M_\odot$ and the fraction of mass in the disk is $\sim 10\%$, equally distributed between the gaseous and stellar component. The contribution of the different components to the global rotation curve, assuming a disk scale length $R_d = 1.7$ kpc and a dark halo concentration $c = 9.5$ (where c is defined as $c = r_{vir}/r_s$, with r_{vir} and r_s virial and scale radius of the NFW halo, respectively) is plotted in Fig. 1. The halo spin parameter, which sets the disk scale length in our modeling, is $\lambda = 0.074$, where λ relates the angular momentum J and the total energy E of a system with virial mass M_{vir} through the relation $\lambda = J|E|^{1/2}G^{-1}M_{vir}^{-5/2}$.

The initial stellar disk of the satellite galaxy has, within its scale radius R_d , a central mass surface density of $\sim 35 M_\odot \text{pc}^{-2}$ (Fig. 2), that corresponds to a B-band surface brightness of $\sim 24 \text{ mag arcsec}^{-2}$, assuming a mass to light ratio $\simeq 2$. The central gas surface density is only $\sim 16 M_\odot \text{pc}^{-2}$ since a significant fraction of gas is distributed in the external disk. Assuming 72% HI abundance this value corresponds to an hydrogen column density of $\sim 1.5 \times 10^{21}$ within R_d , comparable with the values observed by Staveley-Smith et al. (2003) with the LMC Parkes multi-beam HI survey.

2.2 Stability criterium

In order to obtain a strongly stable disk against bar formation even in the presence of significant gas stripping and consequent perturbation of the satellite potential, the thickness of the stellar component is set such that the Toomre's (Toomre 1964) stability criterion is largely satisfied. In particular the Toomre's parameter for the stellar disk:

$$Q_s(R) = \frac{\sigma_r(R)\kappa(R)}{3.36G\Sigma_s(R)}, \quad (3)$$

where $\sigma_r(R)$ is the radial velocity dispersion, $k(R)$ is the local epicyclic frequency and $\Sigma_s(R)$ the unperturbed stellar surface density, has a minimum at the disk scale length with $Q_s(R_d) \sim 4$. For a gaseous disk the stability of the disk is expressed in terms of the gas sound speed v_s and surface density $\Sigma_g(r)$ through the relation:

$$Q_g(R) = \frac{v_s\kappa(R)}{\pi G\Sigma_g(R)}. \quad (4)$$

The gaseous disk has initially a constant temperature of 10000 K, which implies $Q_g(R) > 3$ and $Q(R_d) = 3.2$.

According to Jog & Solomon (1984) and Rafikov (2001), the stability of a multicomponent disk is not guaranteed by the individual stability of its single constituents, due to the mutual gravitational interaction between gas and stars. Stars are characterized by velocity dispersions 3-4 times larger than the typical sound velocities in the cold gaseous disk and even relatively small variations of the

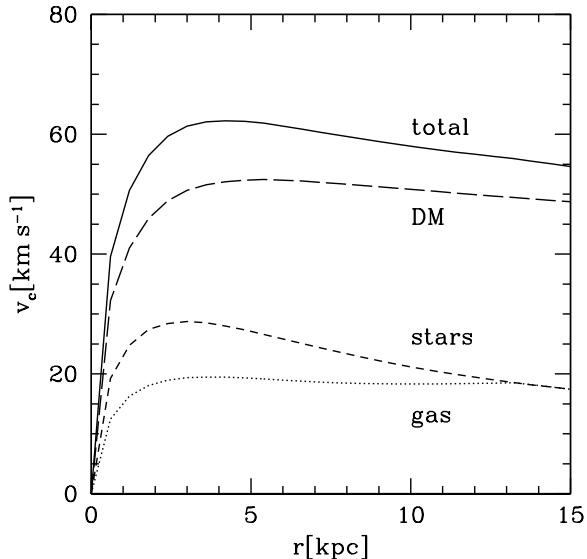


Figure 1. Galaxy model rotation curves.

gaseous component parameters can significantly affect the stability of the whole disk (Jog & Solomon 1984). Therefore we choose a large value of Q to contrast the effects of ram-pressure. In the case of a two components - gaseous and stellar - disk, the stability condition is expressed by (Jog & Solomon 1984)

$$Q_{tot} = \left[\frac{2}{Q_s} \frac{\pi}{3.36} \frac{q}{1+q^2} + \frac{2}{Q_g} x \frac{q}{1+q^2x^2} \right]^{-1} > 1, \quad (5)$$

where $q = k\sigma_s/\kappa$ and $x = c_g/\sigma_s$. Fig. 3 illustrates the dependence of Q_{tot} on the dimensionless wavenumber of the perturbation q within three different regions of the disk: at the disk scale length R_d , at $R = 5$ kpc and in the external region ($R = 8$ kpc), where the gas component predominates. The Jog & Solomon (1984) criterium is always satisfied and the disk is stable against axisymmetric perturbations, independently of their wavelength. In order to check stability the disk was initially evolved in isolation for 1 Gyr.

2.3 Star formation recipes

All the simulations we now discuss were carried out using GASOLINE, a parallel tree-code with multi-stepping (Wadsley, Stadel & Quinn 2004) which is an extension of the pure N-body gravity code PKDGRAV developed by Stadel (2001). The code uses a spline kernel with compact support (Monaghan & Lattanzio 1985) where the interaction distance for a particle i is set equal to two times the smoothing length h_i , defined as the k -th neighbour distance from the particle. In this paper $k = 32$. The internal energy of the gas is integrated using the antisymmetric formulation of Evrard (1988) that conserves entropy closely. Dissipation in shocks is modeled using the quadratic term of the standard Monaghan (1992) artificial viscosity. The Balsara (Balsara 1995) correction term is used to suppress the viscosity in non-shocking, shearing environments. The code includes radiative cooling for a primordial mixture of hydrogen and helium in collisional equilibrium. At temperatures below 10^4

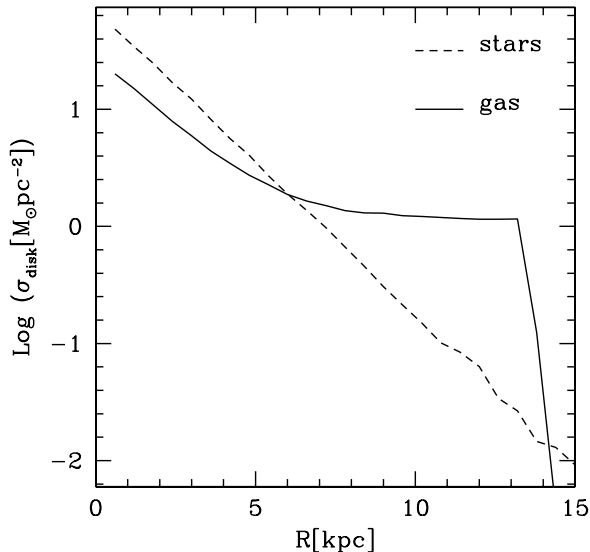


Figure 2. Gaseous and stellar disk surface density profiles (cylindrical coordinates).

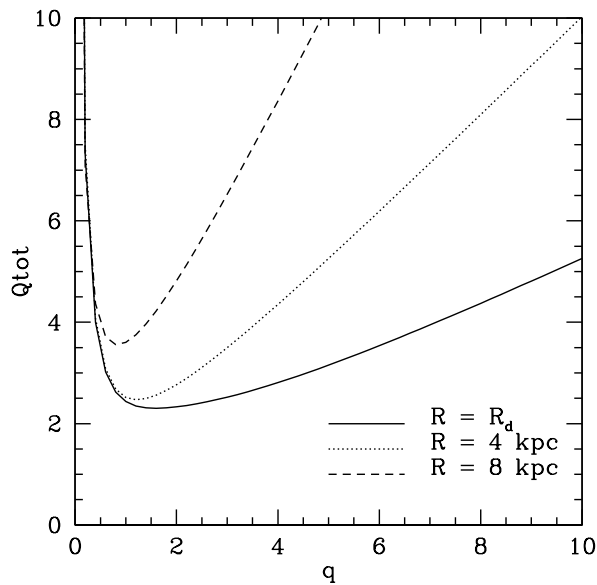


Figure 3. Total stability parameter Q_{tot} of the disk (see Equation 5) versus the dimensionless wavenumber $q = k\sigma_s/\kappa$ of the perturbation. Q_{tot} is calculated for three different radii of the disk.

K the gas is entirely neutral and due to the lack of molecular cooling and metals, the efficiency of the cooling function drops rapidly to zero. We used a star formation recipe that includes density and temperature criteria, while converging flow criterium is not required in most of the simulations. Gas particles are eligible to form stars only if the density of the star formation region has a minimum physical density corresponding to 0.1 hydrogen atoms per cm^3 (Summers 1993; Katz, Weinberg & Hernquist 1996) and an overdensity $\rho_{gas}/\bar{\rho}_{gas} > 55.7$ (Katz et al. 1996), which basically restricts

star formation to collapsed, virialized regions. The physical density threshold describes the steep drop in star formation rate observed in disk galaxies when the gas surface density is much lower than a critical value Σ_c (Kennicutt 1989). The density threshold $\rho_c = 0.1 \text{ cm}^{-3}$ is compatible with observational results. According to Katz (1992), the star forming region has to be part of a converging flow that implies a local negative divergence of the SPH velocity field. However, the converging flow criterium was introduced to describe star formation in cosmological simulations, where the geometry of the collapsing regions is approximately spherical. In the case of star formation regions like 30 Doradus, localized at the periphery of the LMC disk where gas particles relatively close in distance can have significantly different kinematics, this criterium leads to underestimate of the star formation rate. Therefore the converging flow is not required in most of the simulations. A single run including the converging flow requirement has been performed for comparison.

The star formation rate is assumed to be proportional to $\rho_{gas}^{3/2}$ (Silk 1987), where ρ_{gas} represents the volume density of the cold gas, and is given by the expression (Katz, Weinberg & Hernquist 1996)

$$\frac{d\rho_\star}{dt} = \frac{c_\star \rho_{gas}}{t_{form}}, \quad (6)$$

where the star formation timescale t_{form} is the maximum between the local gas dynamical collapse time $t_{dyn} = (4\pi G \rho_{gas})^{-1/2}$ and the local cooling time. If the gas is already cool enough to form stars i.e. $T < T_{max}$, then t_{dyn} is used. We assumed $T_{max} = 30000\text{K}$. The constant star formation rate parameter c_\star is chosen such that we reproduce the global LMC star formation rate (Sandage 1986). Once a gas particle satisfies the above criteria, it spawns stars according to a probability distribution function. In particular, the probability p that a gas particle forms stars in a time Δt is modeled as

$$p = (1 - e^{-c_\star \Delta t / t_{form}}). \quad (7)$$

A random number is then drawn to determine whether the gas particle forms stars during Δt . For all the simulations in this paper $\Delta t = 4 \text{ Myr}$. The newly created collisionless particle has the same position, velocity and softening length as the original gas particle while its mass is a fixed fraction ϵ of the parent gas particle, whose mass is reduced accordingly. Following Katz (1992) we assumed for our favorite models a star formation efficiency $\epsilon = 1/3$. Up to six particles are then created for each gas particle in the disk. After its mass has decreased below 10% of its initial value the gas particle is removed and its mass is re-allocated among the neighbouring particles.

2.4 Test wind tunnels

In order to study the influence of pure ram pressure on a galaxy model orbiting in a Milky Way halo, we performed “wind tunnel” simulations where the ram-pressure value varies with time.

We represent the hot gas as a flux of particles moving along the major axis of an oblong of base equal to the diameter of the dark matter halo of the satellite and height $h = vt$, where v is the velocity of the LMC at the perigalacticon and t is the time scale of the simulation. The hot

particles have an initial random distribution and a temperature $T = 10^6$ K. The box has periodic boundary conditions in order to restore the flow of hot gas that leaves the oblong. The galaxy model is at rest at the center of the oblong.

Kinematical data (van der Marel et al. 2002) indicate that the LMC, presently located at ~ 50 kpc from the Galactic center, is just past a perigalactic passage and has an orbital velocity of about 300 km s^{-1} . Recent proper motion measurements by Kallivayalil et al. (2006) and Piatek et al. (2007) suggest that the velocity of the satellite is substantially higher (almost 100 km s^{-1}) than previously estimated and consistent with the hypothesis of a first passage about the MW (Besla et al. 2007). In both scenarios the Cloud is affected by the largest ram-pressure values during the last million years of its orbital evolution. Indeed, while in the models proposed by Besla et al. (2007) the LMC does not enter the halo of the MW earlier than 1 Gyr ago (slightly different orbits are found in Mastropietro 2008), in M05 we have shown that the change in the orbital parameters due to dynamical friction strongly affects the ram-pressure stripping rate. Even in the case of a “low velocity” model the largest ram-pressure on the satellite is expected during the last orbital semi-period (about 1 Gyr) due to the increasing velocity and external gas density.

We followed ram-pressure acting on the LMC's IGM during the past 1 Gyr. The density of the hot external gas increases with time, in such a way that in our low velocity model the external pressure experienced by the cold disk varies from $P_{min} = \rho_{min} v_{min}^2 = 5 \times 10^{-15} \text{ dyn cm}^{-2}$ to $P_{max} = 1.52 \times 10^{-13} \text{ dyn cm}^{-2}$ at the time corresponding to the pericentric passage. This is equivalent of assuming $v_{min} = 170 \text{ km s}^{-1}$ and $v_{max} \sim 300 \text{ km s}^{-1}$, and a number density of the external gas that increases from $\sim 10^{-5} \text{ cm}^{-3}$ to 10^{-4} cm^{-3} at ~ 50 kpc from the Galactic center. These density values are comparable with those provided by M05, who modeled the MW hot halo assuming a spherical distribution of gas that traces the dark matter profile, with a mean number density of 2×10^{-5} within 150 kpc. We also consider the eventuality of a less dense Galactic halo and performed runs where the gas density is a factor 10 lower. Models with higher velocities (Kallivayalil et al. 2006) and orbital parameters similar to those suggested by Besla et al. (2007) are also explored. In details, P_{min} is the same as in the low velocity models since the higher orbital velocity at the beginning of the simulation (about 250 km s^{-1}) is compensated by a lower external density ($\sim 5 \times 10^{-6} \text{ cm}^{-3}$, according to Mastropietro 2008. Indeed 1 Gyr ago the satellite has just passed through the virial radius of the MW). The maximum pressure felt by the disk is $P_{max} = 2.67 \times 10^{-13} \text{ dyn cm}^{-2}$, that corresponds to a Cloud moving with $v_{max} \sim 400 \text{ km s}^{-1}$ through an external hot medium of density 10^{-4} cm^{-3} .

Each galaxy model is simulated using 750000 particles, of which 6×10^5 are in the dark halo and 1.5×10^5 in the disk (10^5 collisional and 5×10^4 collisionless). The hot gas in the “wind tunnel” has 2×10^6 particles, in such a way that the mass ratio m_h/m_{disk} between hot particles and particles in the disk is close to the unity even when the halo density is the largest. This choice permits to avoid the presence of scattering and numerical holes which artificially change the shape of the front edge and influence the morphology of the disk (M05). The gravitational spline softening is set equal

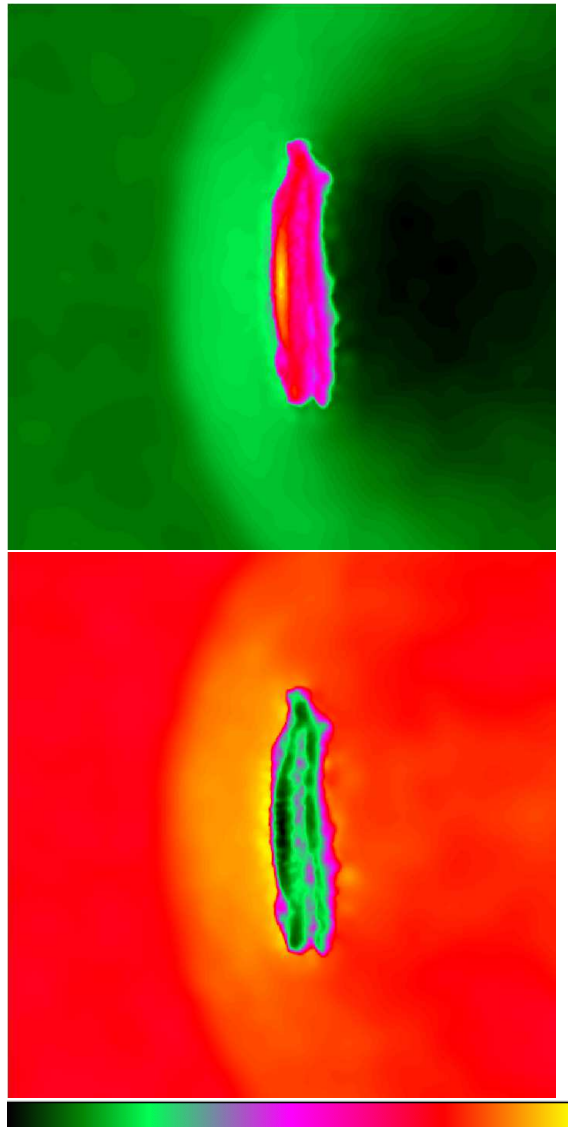


Figure 4. Density (upper panel) and temperature (bottom) map of a $50 \times 50 \text{ kpc}^2$ region around the satellite, which is moving towards the left of the page nearly face-on (inclination angle $i = 10^\circ$, cool10). Logarithmic color scaling is indicated by the key at the bottom of the figure. The surface density map ranges between $\sim 2 \times 10^3$ (black) and $\sim 2 \times 10^9 \text{ M}_\odot \text{ kpc}^{-2}$ (yellow), while temperatures vary from 10^4 (black) to 10^7 K (yellow).

to 0.5 kpc for the dark halo and the hot gas in the oblong, while it is 0.2 kpc for stars and gas in the disk.

3 COOLING SIMULATIONS

In order to study the effect of pure compression on the density distribution of cold gas in the LMC disk, we have run a first set of simulations where the gas cools radiatively but star formation was not activated.

According to van der Marel et al. (2002) and Kallivayalil et al. (2006), the present angle between the LMC's disk and its proper motion vector is roughly 30° . Even neglecting the effects of precession and nutation on the disk plane of the satellite (van der Marel et al. 2002)

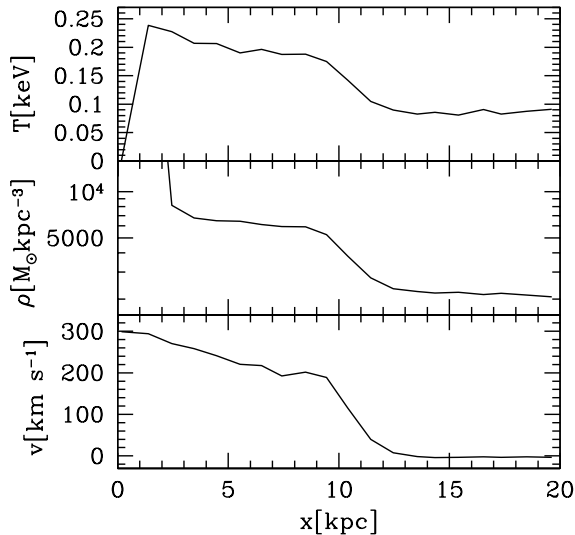


Figure 5. Gas temperature (top panel), density (middle) and one dimensional velocity (bottom) profiles across the shock discontinuity.

this angle is expected to vary significantly during an orbital period, especially in the proximity of a pericentric passage due to rapid changes in the velocity vector. Different relative orientations of the disk with respect to the orbital motion are therefore investigated. The inclination angle i is defined as the angle between the angular momentum vector of the disk and the flux of hot particles in the wind tube, so that a galaxy moving edge-on through the external medium is characterized by $i = 90^\circ$, while the observed LMC disk would have $i \sim 60^\circ$. We explored cases with inclination angle i of 90, 45 and 10° (runs cool90, cool45 and cool10, respectively).

With a hot halo temperature of 10^6 K the relative velocity between the satellite and the external medium is supersonic (sound speed ~ 135 km s $^{-1}$ and Mach number $\mathcal{M} = 2.2$ and 3 at the pericenter of the low and high velocity orbit, respectively) and a bow shock forms in front of the disk (Fig. 4). Since the cooling time of the post-shock gas is ~ 16 Gyr, the shock can be considered adiabatic and hydrodynamical quantities at the two sides of the shock front are in first approximation related by the Rankine-Hugoniot equations for a stationary normal shock.

For $\mathcal{M} > 1$ the jump conditions give $\rho_1/\rho_2 = v_2/v_1 < 1$ and $T_1 < T_2$, where subscripts 1 and 2 denote upstream and downstream quantities. The ram-pressure $P_2 = \rho_2 v_2^2$ actually felt by the galaxy behind the shock front is therefore smaller than that it would suffer due to the upstream flux of hot particles, but conservation of momentum flux across the shock discontinuity implies that the reduction in dynamical pressure has to be balanced by an increase in thermal pressure (see also Rasmussen et al. 2006).

Fig. 5 illustrates the behavior of hydrodynamical quantities across the shock discontinuity for a snapshot corresponding to the perigalacticon of a low velocity orbit. The disk inclination is $i = 10^\circ$. The horizontal axis is centered on the LMC stellar disk and oriented perpendicularly to

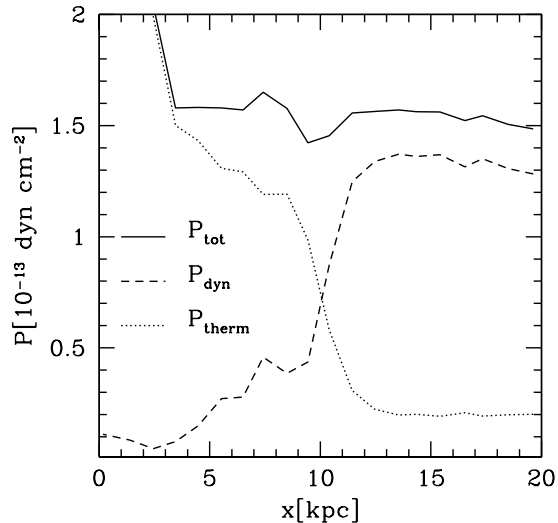


Figure 6. Dynamical (P_{dyn}), thermal (P_{therm}) and total (P_{tot}) pressure across the shock.

the bow shock nose, with the shock located at $x \sim 10$ kpc and the satellite moving towards increasing values of x . The Mach number derived by the temperature jump is $\mathcal{M} = 2.1$, in good agreement with the theoretical value for a normal shock. Only hot halo particles are considered in computations but, due to the SPH nature of the simulations, close to the border of the disk we observe a further density increase and a sharp drop in temperature. The x -velocity profile is plotted in the system of reference where the pre-shock gas is at rest.

Pressure profiles across the shock are plotted in Fig. 6, where P_{dyn} is defined as ρv^2 . The total pressure remains roughly constant until the edge of the disk. The step increase at $x = 2.5$ kpc is due the rapid growth in density at the border of the disk, which is not immediately followed by a decrease in temperature.

For $i > 0^\circ$ the shock wave is inclined with respect to the initial flow velocity and the Rankine-Hugoniot conditions apply to the normal components of the velocity across the shock discontinuity, while the component parallel to the shock front remain unchanged. The flow is therefore deflected toward an oblique shock wave and the jump at the shock discontinuity is smaller.

An edge-on ($i = 90^\circ$) disk behaves like a wedge moving supersonically with the vertex facing upstream. If the wedge angle is smaller than or equal to the maximum flow deflection angle, the oblique shock becomes attached to the vertex of the wedge and the flow is deflected so that the streamlines are parallel to the surfaces of the wedge. The shock stand-off distance thus depends on the external density profile of the collisional edge-on disk and on the Mach number of the incident flow. In both low and high velocity edge-on models the shock results almost attached to the disk.

Figs. 7–9 illustrate – for different values of the inclination angle i – changes in the disk gas density distribution as the satellite passes through increasing values of the external pressure, moving towards the perigalacticon. Each couple of

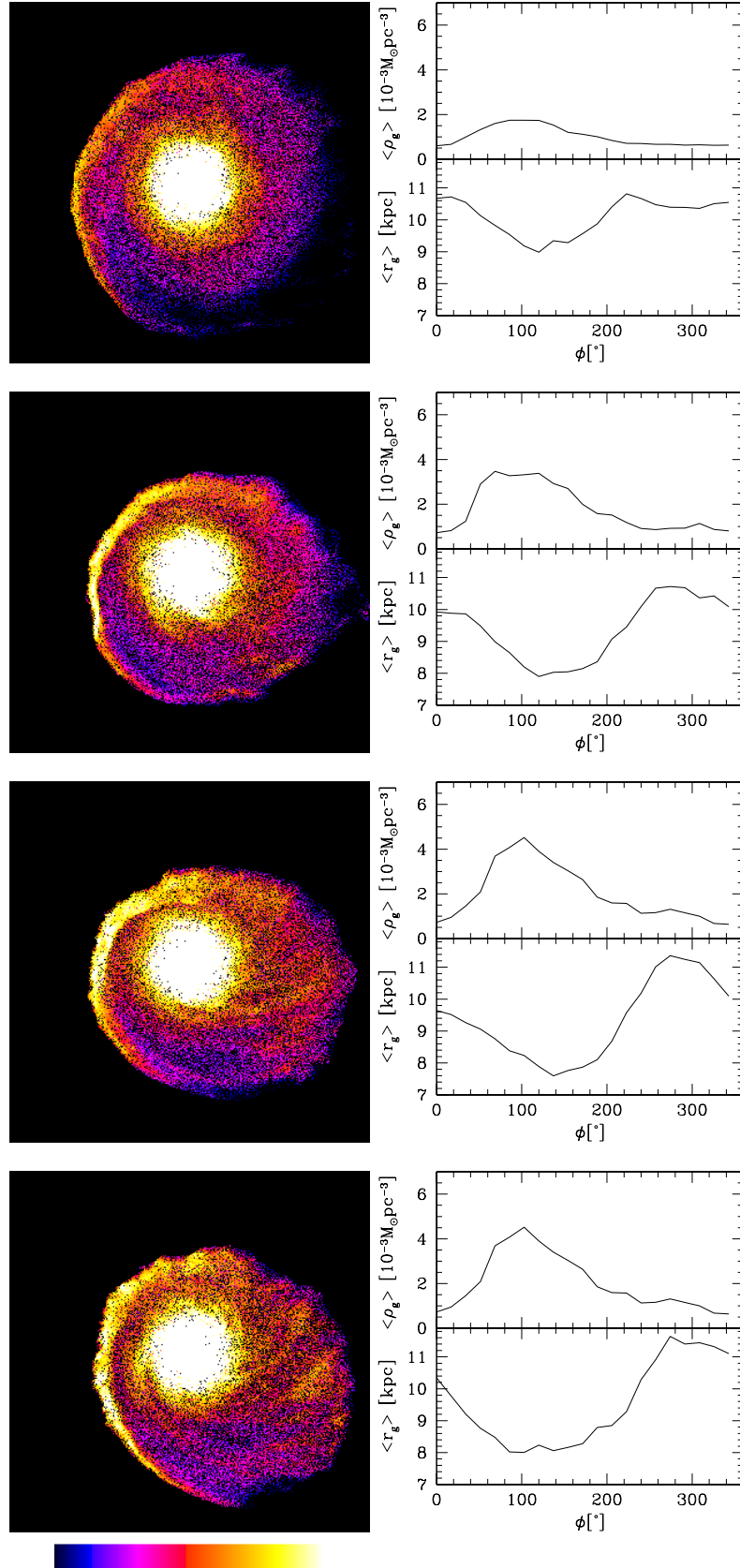


Figure 7. Edge-on model (run cool90). Evolution of the disk gas density distribution. Left panels: HI column density maps (the galaxy is moving towards the left of the page). The color-scale is logarithmic with limits 5×10^{19} and $1.2 \times 10^{21} \text{ cm}^{-2}$. Right panels: mean gas density and radius of the external disk as a function of the azimuthal angle ϕ . Each pair of plots (from the top to the bottom) represents the state of the disk at increasing times along the orbit: Time= 0.4, 0.6, 0.8, 1Gyr.

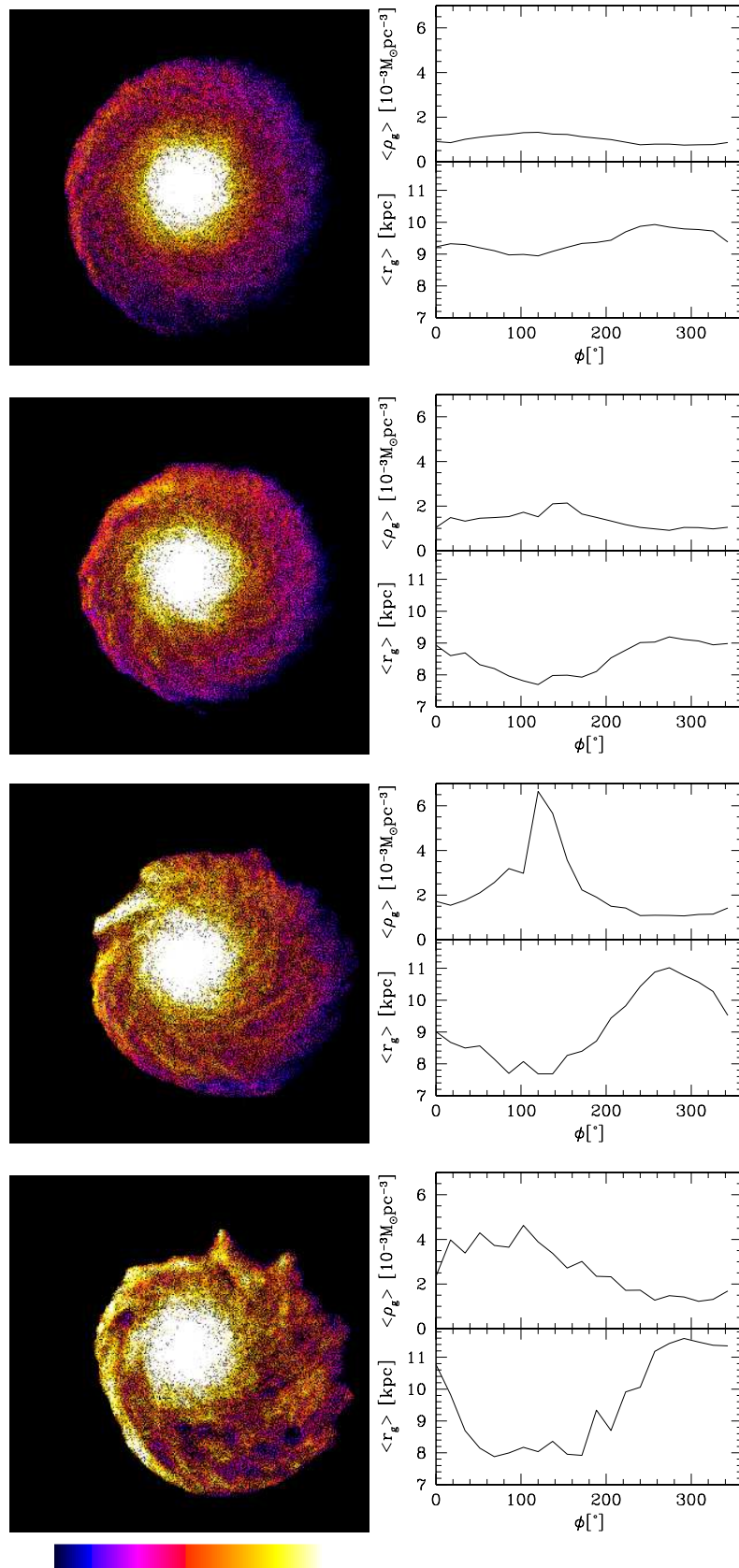


Figure 8. The same as in Fig. 7 for the model with inclination angle $i = 45^\circ$ (run cool45)..

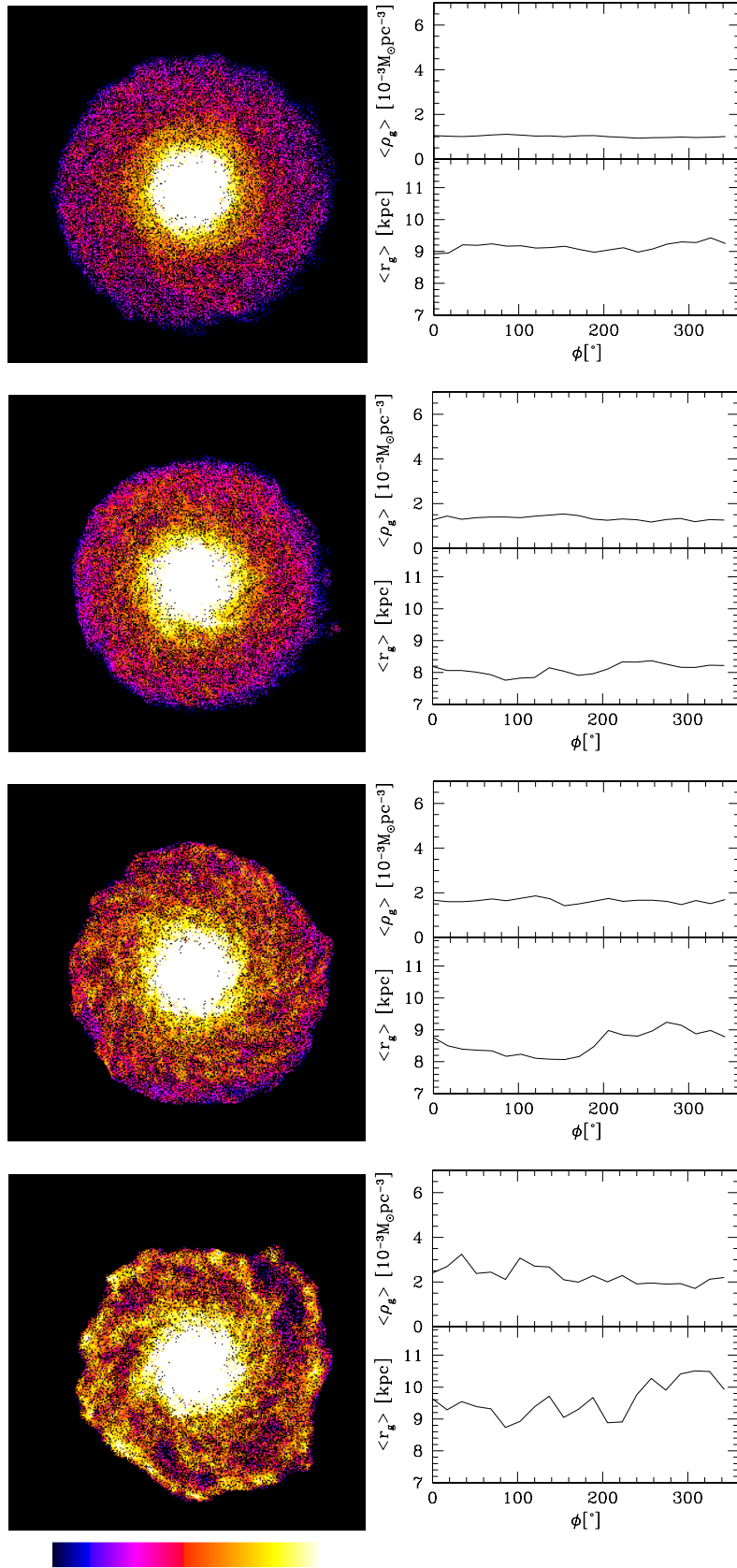


Figure 9. The same as in Fig. 7 for the model with inclination angle $i = 10^\circ$ (run cool10).

panels illustrates the state of the disk at increasing (from the top to the bottom) times along the orbit. Panels on the left represent HI column density maps. The density contrast is chosen in order to highlight the density gradient in the external disk, since the gas distribution in the central regions of the LMC is dominated by the presence of the bar and a direct comparison with pure ram-pressure simulations is not possible. The color scale is logarithmic, with white corresponding to a density larger than $1.2 \times 10^{21} \text{ cm}^{-2}$ and blue to values lower than $5 \times 10^{19} \text{ cm}^{-2}$. Hot gas particles flow on to the disk from the left to the right of each plot, with increasing ram-pressure values from the first to the fourth image. The disk is seen face on and rotating clockwise. In the case of the edge-on run (Fig. 7) cold gas particles lying in the left-bottom quadrant of the disk feel the largest ram-pressure, due to the fact that their relative velocity with respect to the external medium is maximum. The rotational velocity of the external disk is $\sim 55 \text{ km s}^{-1}$, which implies a relative velocity at the pericenter of $\sim 350 \text{ km s}^{-1}$ (450 km s^{-1} in the case of a high velocity orbit). Panels on the right represent the change in mean density and radius of the gaseous external disk as a function of the azimuthal angle ϕ . Referring to the geometry of the HI density images on the left, $\phi = 0^\circ$ corresponds to the bottom of the disk and increases clockwise in such a way that the disk moves in the direction of $\phi = 90^\circ$. The gas density and the mean radius are both calculated within sections of a three dimensional annulus with internal and external radius equal to 7 and 15 kpc, respectively. The initial azimuthal profiles (not represented in the plots) are flat since both these quantities have only radial dependence. As soon as the satellite starts moving through the surrounding medium, the external gas density develops a peak centered on $\sim \phi = 90^\circ$: disk particles localized in regions of maximum ram-pressure get compressed and move on inner orbits, while their circular velocity increases consequently. After about a quarter of the orbital period the gas has reached its minimum radius and maximum local density. The gaseous disk becomes strongly asymmetric: compression at the front edge produces a density increase along the left border of the disk, evident in the HI maps even at early times. The high density region forms a thin ($\sim 1.5 \text{ kpc}$) but continuous and well defined arc which has not an equivalent in the stellar distribution. At the perigalacticon this feature extends for almost 160° with a density more than one order of magnitude higher than gas located at smaller radii. Its average thickness ($\sim 1.5 \text{ kpc}$) and velocity dispersion along the line of sight are larger than the average values in the rest of the disk.

In the case of a satellite moving through the hot medium with an inclination angle different from 90° the external pressure directed perpendicularly to the plane of the disk increases as $\cos i$ (Roediger & Brügger 2006) while compression at the leading edge is much less pronounced. Figs. 8 and 9 refer to runs with inclination angles $i = 45^\circ$ and $i = 10^\circ$. Disks are shown face-on. The increment in density along the leading edge is smaller (cool45) than in the edge-on model and almost absent for $i = 10^\circ$ (cool10), while compression perpendicular to the plane of the disk produces local gravitational instabilities in the external gaseous disk (also Mayer, Mastropietro & Tran in preparation). This effect is more evident in the nearly face-on run cool10 where high density filaments delimitate regions where the local density is almost

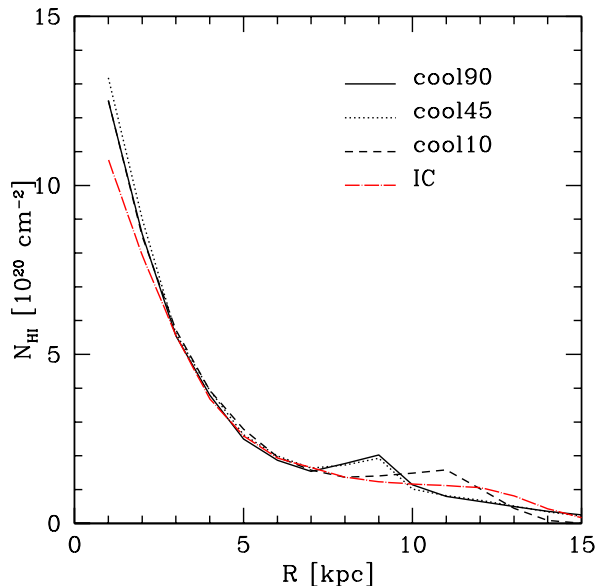


Figure 10. HI column density profile of the final LMC disk in units of 10^{20} cm^{-2} . The curves refer to different values of the inclination angle i . The red long-dashed line represents the column density profile of the initial disk.

one order of magnitude lower. Despite the absence of a peak in the azimuthal mean density profile, the integrated final density of cool10 is comparable to the other runs.

Fig. 10 represents the azimuthally averaged HI column density profile of the final disk configuration for the three simulations. As a result of the increase in density along the edge of the disk, the mean column density shows a secondary peak at large radius. A limb-brightened density profile has actually been observed by Staveley-Smith et al. (2003) using the Parkes multibeam HI survey of the LMC. The outer profiles of cool90 and cool45 are very similar, while in run cool10 the increment in density with respect to the original profile of the disk (long-dashed red curve in the plot) is located at larger radii ($\sim 8.5 \text{ kpc}$). Indeed, due to compression of the leading edge the final gas distribution of cool90 and cool45 is asymmetric, the dense front edge being much closer to the center than the opposite border of the disk. Therefore the HI peak in the external disk is located at relatively small radii, while the azimuthally averaged gas distribution is more extended than in the case of the run cool10 since ram pressure elongates the back side of the disk. Again we stress the fact that our gaseous disk is more extended than it would be in a fully self consistent simulation including both gravitational and hydrodynamical forces. As seen in M05 and Mastropietro (2008) the combined effect of ram-pressure and tidal stripping is quite efficient in stripping gas from the outer satellite's disk, creating the tip of the Magellanic Stream already at large distances from the MW. The high density feature in cool90 would then form along the border of the disk at smaller radii and would not be easily subjected to further stripping due to the relatively ram-pressure values.

Table 1. Star formation simulations. The second column indicates the use of the converging flow criterium in the star formation recipe, the third and the fourth columns represent the star formation efficiency ϵ and the star formation rate parameter c_* (Eq. 6), respectively, while i is the inclination angle of the disk, i.e. the angle between the angular momentum of the disk and the flux of hot particles. A model with $i = 90$ is indeed a disk moving edge-on in the external medium. The sixth and seventh columns represent the minimum and maximum ram pressure suffered by the satellite during its approach to perigalacticon. The last column indicates the presence of a temperature floor for the disk gas.

Run	conv	ϵ	c_*	i	[$^\circ$] P_{min} [10^{-13} dyn cm $^{-2}$]	P_{max} [10^{-13} dyn cm $^{-2}$]	T_{min} [kelvin]
SF90	no	0.33	0.02	90	4.83×10^{-2}	1.50	0
SF45	no	0.33	0.02	45	4.83×10^{-2}	1.50	0
SF10	no	0.33	0.02	10	4.83×10^{-2}	1.50	0
SFconv	yes	0.33	0.02	90	4.83×10^{-2}	1.50	0
SF ϵ 1	no	1	0.02	90	4.83×10^{-2}	1.50	0
SFconv ϵ 1	yes	1	0.02	90	4.83×10^{-2}	1.50	0
SF90c0.01	no	0.33	0.01	90	4.83×10^{-2}	1.50	0
SF10c0.01	no	0.33	0.01	90	4.83×10^{-2}	1.50	0
SF90c0.05	no	0.33	0.05	90	4.83×10^{-2}	1.50	0
SF10c0.05	no	0.33	0.05	90	4.83×10^{-2}	1.50	0
SF90v400	no	0.33	0.02	90	4.83×10^{-2}	2.67	0
SF10v400	no	0.33	0.02	10	4.83×10^{-2}	2.67	0
SF10v400t12000	no	0.33	0.02	10	4.83×10^{-2}	2.67	1.2×10^4
SF10v400t15000	no	0.33	0.02	10	4.83×10^{-2}	2.67	1.5×10^4
SF1d90	no	0.33	0.02	90	4.83×10^{-3}	1.5×10^{-1}	0
SF1d10	no	0.33	0.02	10	4.83×10^{-3}	1.5×10^{-1}	0

4 SIMULATIONS WITH STAR FORMATION

The compressive increase in HI density is naturally associated with excess star formation. SPH simulations cannot follow the formation of molecular clouds but in first approximation the molecular gas fraction can be related to the density of atomic gas (Vollmer et al. 2008).

The main parameters of star formation simulations are summarized in Table 1.

As we already mentioned in Section 3, our standard star formation model (SF) does not include the converging flow criterium and is characterized by an efficiency $\epsilon = 0.33$ (Katz 1992). The star formation rate parameter c_* is initially set equal to 0.02. This model was adopted to run wind tube simulations with inclination angles $i = 90, 45, 10^\circ$ (SF90, SF45, SF10) (Table 1). We also investigated different star formation recipes requiring converging flows and assuming different values of c_* and ϵ . We explored star formation rate parameter values in the range from 0.01 to 0.05, that produce a star formation rate integrated over the entire disk comparable with the $0.1M_\odot \text{ yr}^{-1}$ provided by Sandage (1986). An efficiency $\epsilon = 1$ implies that whenever a gas particle satisfies the star formation requirements, it is immediately turned into a single star particle of the same mass (Kaufmann et al. 2006).

In the last six simulations listed in Table 1 we used our standard star formation model SF to investigate the effects of different orbital parameters and gas halo densities.

Runs SFv400 are characterized by a maximum ram pressure value corresponding to a perigalactic velocity of 400 km s $^{-1}$ (Kallivayalil et al. 2006). Such high velocity disks – when moving face-on through the external hot medium – are strongly affected by local instabilities and star formation is consequently enhanced. The introduction of an artificial lower limit for the satellite gas temperature (in runs SF10v400t12000 and SF10v400t15000), higher than the cut-off in the cooling function, has the effect of reducing grav-

itational instabilities and fragmentation in the disk. This temperature threshold can be justified in order to crudely model the effect of the UV background and stellar feedback (Barnes 2002).

Finally, with simulations SF90ld and SF10ld in Table 1 we also consider the possibility of a Galactic hot halo ten times less dense than our standard model.

Fig. 11 illustrates the state of the newly formed stellar disk at increasing times along the satellite orbit. Each couple of rows corresponds to one of the first three runs of Table 1 and is associated with a different inclination angle i . The first row of the pair represents the face-on projection of the disk with the galaxy moving towards the left of the page and the same geometry as in Fig. 7. Time increases from the left to the right. Each small cross indicates a new star formation event at the time of the snapshot (within a time interval of 40 Myr) while the circle delimitates the external disk ($r > 7$ kpc). Stars form in the central regions as soon as the star formation algorithm is activated, but here the star formation activity of the inner disk is not represented. The second row represents the total mass M_* of the newly formed stars in the external disk as a function of the disk azimuthal angle ϕ .

In the case of a galaxy moving edge-on through the external medium (SF90), stars form at the leading edge of the disk when the ram-pressure becomes larger than $\sim 5 \times 10^{-14}$ dyn cm $^{-2}$, at Time ~ 0.3 Gyr. The location of the star formation events initially corresponds to the HI column density peak observed in cool90 around 100° (Fig. 7). Later on it expands along the entire front edge, creating a thin stellar arc well distinct from the star formation events that characterize the central disk. As soon as the satellite encounters ram pressure values comparable to those experienced by the LMC at the perigalacticon (Time $\gtrsim 0.6$ Gyr) some episodes of star formation occur even on the back side of the disk (last plot on the top right of Fig. 11), although they are

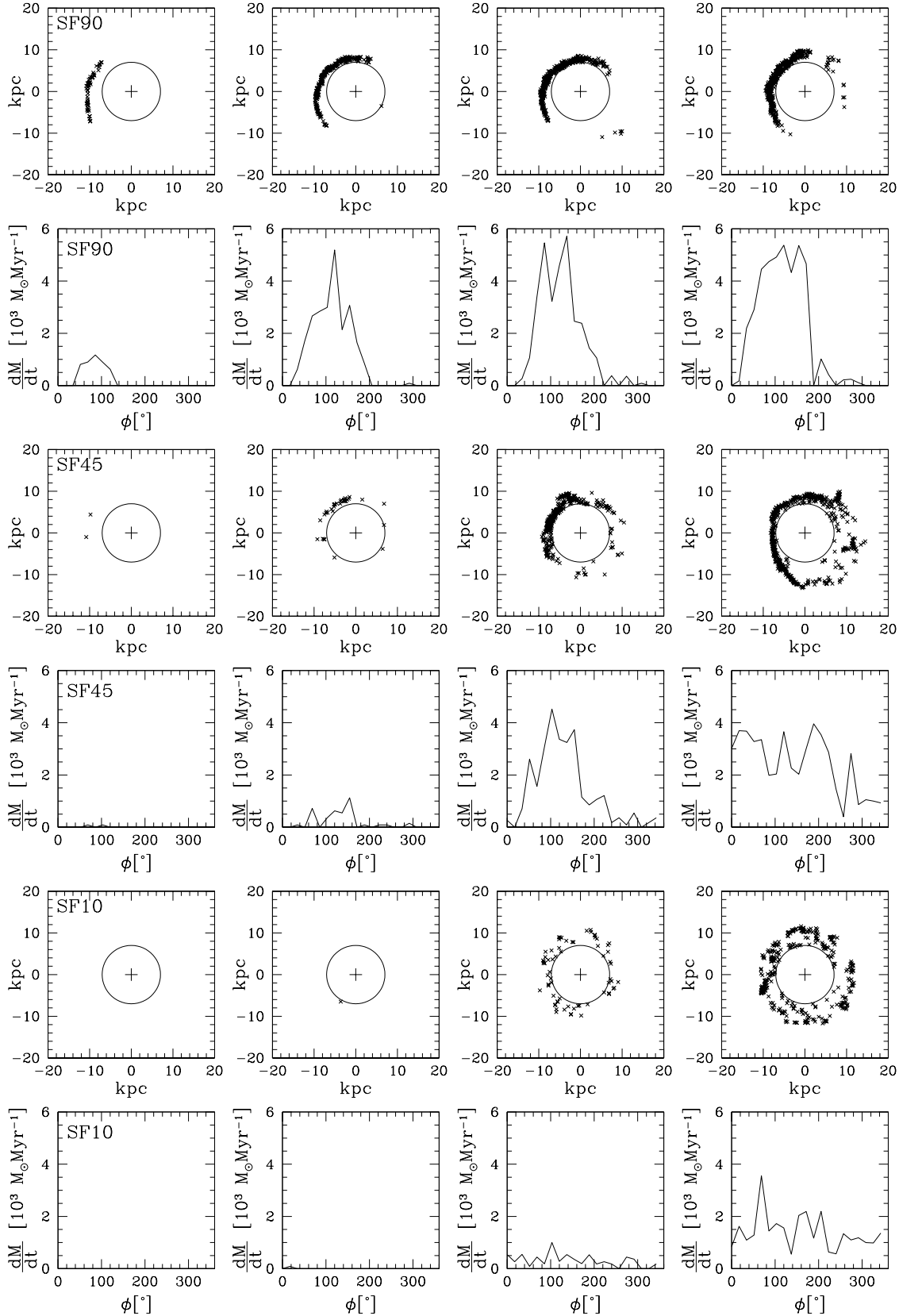


Figure 11. Location of the instantaneous star formation events in the external disk. Each couple of rows corresponds to a different inclination angle of the disk. Time increases from the left to the right: Time=0.4,0.6,0.8,1 Gyr. The first row of the couple represents the disk face on projection, the second one the star formation rate versus the azimuthal angle ϕ .

not relevant in terms of new stellar mass formed. Indeed M_* shows a drastic drop at $\phi = 200^\circ$.

Runs with inclination $i < 90^\circ$ are characterized by significant star formation only for values of the external pressure larger than 10^{-13} dyn cm $^{-2}$. In the case of the nearly face-on run SF10, at $t > 0.7$ Gyr star formation occurs in the entire external disk. Ram-pressure affects the plane of the disk almost perpendicularly and stars form along the delocalized and filamentary high density structures visible in Fig. 9 (Mayer et al. in prep.). Contrary to what has been found by Kronberger et al. (2008) who focused on higher ram-pressure values ($n \sim 10^{-4}$ cm $^{-3}$ and $v = 1000$ km s $^{-1}$) typical of the outskirts of galaxy clusters, the newly formed stars are all located in the plane of the satellite's disk (with the exception of the high velocity face-on run SF10v400 where about 10% of the stars forms behind the disk). The star formation events appear to be distributed nearly homogeneously along the azimuthal profile of the external disk, although a small peak in M_* is observable near $i = 90^\circ$. In fact, the orientation of the disk with respect to its orbital motion is not exactly face-on. The case of the intermediate run SF45 is more complex. In a first phase, for low ram pressure values, star formation is produced by compression at the leading edge and a thin star formation front – although not so well defined as in the case of a pure edge-on model – appears on the east side of the disk. As soon as the external pressure reaches a critical level compression directed perpendicularly to the disk becomes the dominant mechanism driving star formation.

Converting SFRs to H α luminosities according to Kennicutt (1998):

$$L(H\alpha) = \frac{\text{SFR}(M_\odot \text{yr}^{-1})}{1.26 \times 10^{41}}, \quad (8)$$

where SFR is the star formation rate averaged over the last 40 Myr (nearly two times the stellar age of 30 Doradus), we obtain the H- α maps illustrated in Fig. 12.

High emission regions are mainly concentrated in the external disk (with the exception of run SF1d90 where the ram-pressure exerted by the low density halo is not enough to induce star formation at the edge of the disk). The continuous stellar arc forming along the leading side of the disk in edge-on runs breaks up into several distinct and very luminous H- α regions that more closely resemble the star-forming complexes observed on the eastern border of the LMC. The inclusion of stellar and supernovae heating – which has been neglected in the present simulations – could prevent further star-formation around highly emitting regions and consequently produce more compact and isolated star-forming complexes. Nevertheless, modeling single star-formation complexes – whose linear extension is smaller than our softening length – is beyond the scope of this paper.

The present inclination of the LMC's disk with respect to the orbital motion is about 60° (according to the convention adopted in this paper). Since the satellite is currently near a perigalactic passage we expect the H- α map at the leading border of the disk to be something in between pure edge-on runs and the run with inclination of 45° . On the other side, it is very likely that the disk inclination during the phase of approach to the pericenter was different. Indeed in Mastropietro (2008) we have simulated the LMC's

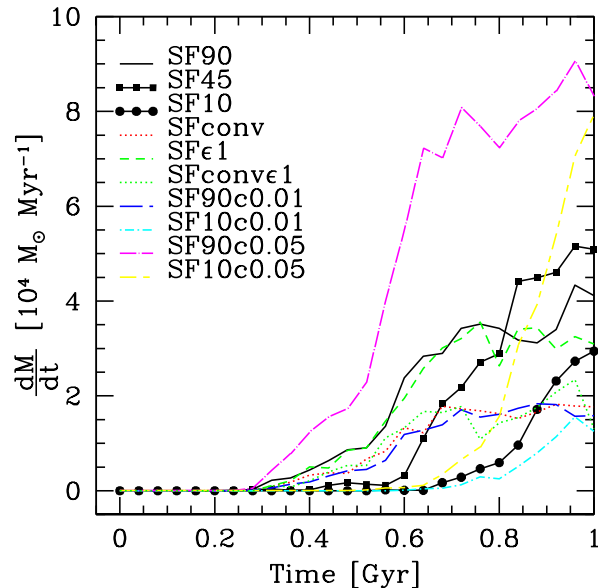


Figure 13. Star formation rate of the external disk ϕ for the first ten runs listed in Table 1. Time increases approaching to the present position.

orbit according to the new proper motion measurements of Kallivayalil et al. (2006) and found that the cloud enters the MW halo face-on and moves almost face-on during most of the last 1 Gyr. It turns nearly edge-on only at the perigalacticon. This would have a remarkable effect on the star-formation history of the external disk during the last 1 Gyr and some impact also on the H- α maps. Indeed, although the H- α emission would be mostly concentrated on the eastern side of the disk due to the very recent edge-on motion, we expect to see some luminous clumps forming a patchy distribution on the entire disk, due to gravitational instabilities and subsequent star-formation induced by a nearly face-on compression of the gaseous disk before 30 Myr ago.

The high velocity edge-on run SF90v400 presents a more elongated and thinner stellar arc along the leading border, with a geometry similar to that obtained increasing the star formation rate parameter to 0.05 (SF90c0.05). The H- α map of SF90v400 (third panel of the third row) shows two distinct luminosity peaks. One is located at the south-east region of the disk, roughly corresponding to the position of 30Doradus and the two compact emission regions N159 and N160.

Fig. 13 illustrates how the star formation rate of the external disk changes with time in the different models. The three black curves refer to the standard star formation runs SF, characterized by low orbital velocities. The edge-on disk starts forming stars earlier, but for large ram pressure values the star formation rate of SF10 and SF45 grows faster. At the perigalacticon passage SF45 has indeed a higher star formation rate than SF90. In the case of an isolated LMC model star formation is almost absent for $r > 7$ kpc. The remaining curves in Fig. 13 refer to different star formation recipes (rows 4-9 of Table 1). The location of the star

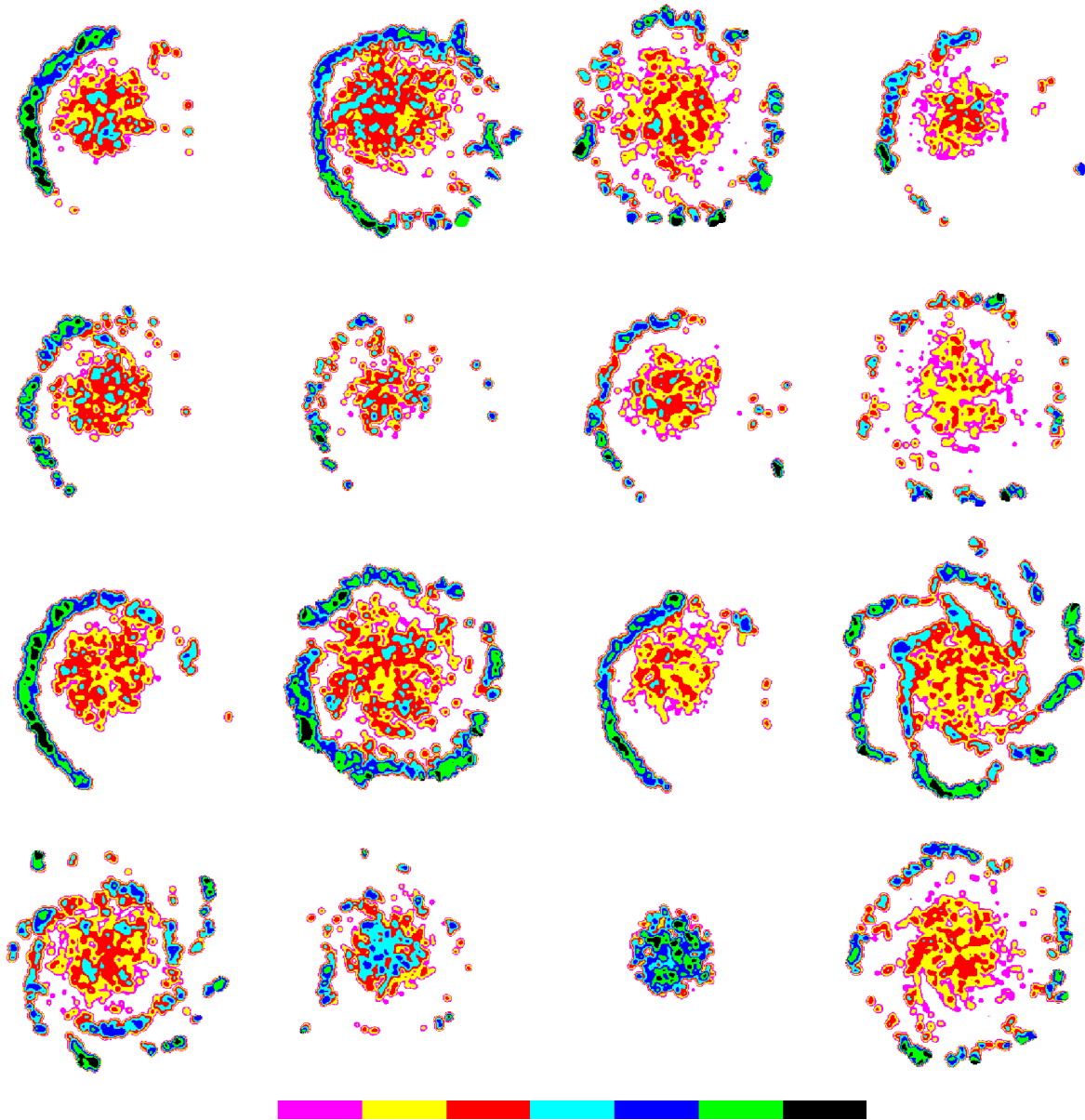


Figure 12. H- α maps of the LMC's disk. The different panels represent (from top to bottom and from left to right) runs listed in Table 1: SF90, SF45, SF10, SFconv, SF ϵ 1, SFconv ϵ 1, SF90c0.01, SF10c0.01, SF90c0.05, SF10c0.05, SF90v400, SF10v400, SF10v400t12000, SF10v400t15000, SF1d90, SF1d10. The color-scale is logarithmic with limits 10^{31} and 10^{34} erg s $^{-1}$ kpc $^{-2}$.

formation events in the external regions of the disk does not change significantly choosing different parameters in the star formation algorithm. The star formation rate parameter c_* determines the amount of new stars forming but does not affect the minimum threshold in ram-pressure neither the evolution of the star formation rate. In particular, in the case of edge-on runs after an initial step increment the curve seems to converge to a constant value for increasing external pressures. The consequences of an increased star formation efficiency (ϵ 1) are almost negligible (but not in H α maps where only the very recent star formation rate is taken in account: compare the first panels of the first and second row) while including the convergence requirement

(SFconv) has nearly the same effect than reducing the star formation rate parameter of a factor two.

For convenience, the star formation rate of the last six runs of Table 1 is plotted separately (Fig. 14). The high velocity edge-on model SF90v400 is characterized by a steeper increment in star formation at earlier times but later on the curve flattens and the star formation rate at the perigalacticon is similar to that of the low velocity case SF90. Differences in H- α maps are produced by a difference of $\sim 5 \times 10^3 M_\odot \text{ Myr}^{-1}$ about Time = 1 Gyr. On the contrary, the star formation generated by compression perpendicular to the disk increases with increasing ram-pressure values (it shows a decrement only towards the end of the simulation) and in the case of the high velocity run SF10v400 reaches a

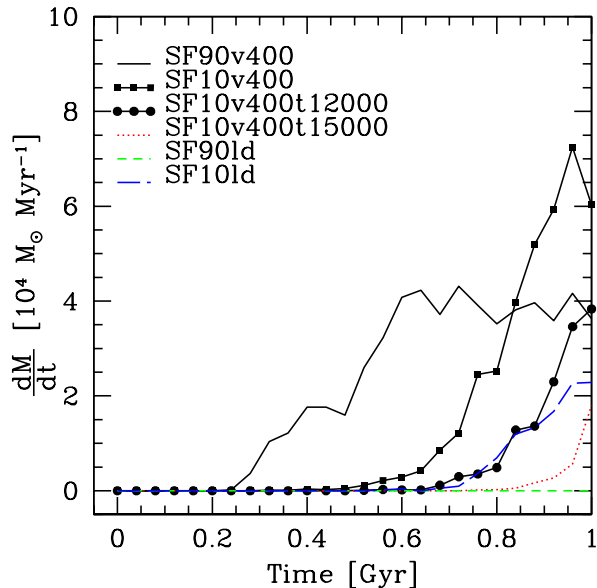


Figure 14. Same as in 13 for the last six runs listed in Table 1.

peak ~ 1.5 times higher than in SF10. The star formation rate of SF10v400 is strongly affected by the introduction of an artificial temperature threshold. With a temperature floor of 15000 K we nearly suppress star formation in the external disk. However, a threshold of 12000 K is already very high for a LMC model and more typical of luminous disk galaxies like the MW. A temperature floor lower than 10000 K would not make sense since below this temperature the cooling function adopted in the present paper drops rapidly to zero. If, as pointed out by Mastroiello (2008), the satellite is moving almost face-on until it gets very close to perigalacticon, we would not expect to see star formation before 0.6 Gyr independently of the orbital velocity. Differences between high and low velocity runs should be marginal also near the pericenter since star formation in edge-on runs – assuming our standard prescriptions for star formation – seems to saturate around $\sim 4 \times 10^4 M_{\odot} \text{ Myr}^{-1}$. Finally, a hot halo ten times less dense than the one assumed in our favorite model would reduce drastically the star formation in a face-on LMC and suppress completely the star formation on the leading edge of the disk.

The star formation rate of the entire disk is illustrated in Fig. 15. This plot is only indicative since we neglect the presence of the bar and its influence on the star formation history of the satellite. The star formation rate of a LMC model evolved in isolation is plotted for comparison. The largest contribution to SFR is given by star formation events in the central region of the disk. Curves peak between 15 and $35 M_{\odot} \text{ Myr}^{-1}$, comparable with observations of the Magellanic Clouds Photometric Survey (Harris et al. in prep). The total star formation rate is clearly not affected by ram-pressure before 0.4 Gyr. Indeed, after an initial sharp increment curves are rather flat despite orientation and intensity of the external pressure. An initial burst in star formation is obtained only by increasing the star formation efficiency pa-

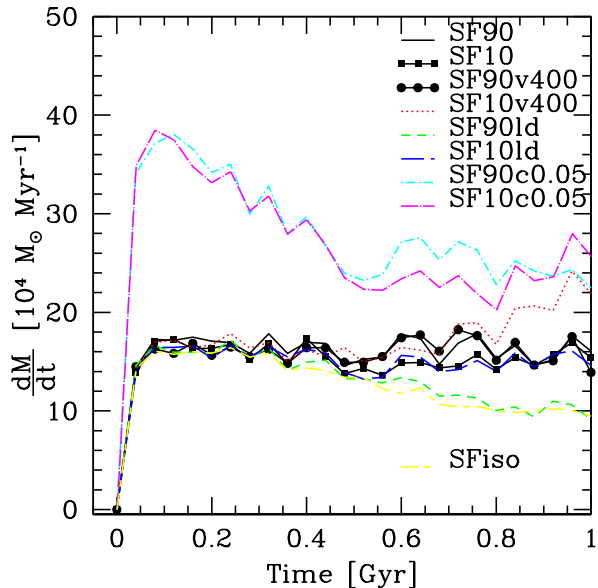


Figure 15. Star formation rate of the entire disk for selected runs in Table 1. SFiso refers to the LMC model run in isolation.

rameter to 0.05. For $\text{Time} > 0.5 \text{ Gyr}$ the largest deviations from an average star formation rate of $\sim 15 M_{\odot} \text{ Myr}^{-1}$ are produced in the edge-on low density run SF90ld, where dM/dt drops to $10 M_{\odot} \text{ Myr}^{-1}$ at $\text{Time} = 1 \text{ Gyr}$, and in the high velocity face-on model SF10v400 whose star formation rate increases up to $\sim 24 M_{\odot} \text{ Myr}^{-1}$ toward the end of the simulation. Differences among the other models are of the order of few $M_{\odot} \text{ Myr}^{-1}$ and vary with time so that it would be quite difficult to use the star formation history of the entire disk to test the Cloud's orbital parameters and the hot halo density.

Fig. 17 represents the mean stellar age of the external disk versus the azimuthal angle ϕ for the same selected runs of Fig. 15. The maximum increment in age in a clockwise direction is associated with edge-on runs, where stars forming at the leading edge move, in time, away to the side, due to the clockwise rotation of the disk. The youngest stars are located at $30^{\circ} < \phi < 100^{\circ}$. Clearly the gradient in age is much weaker in models with $i < 90^{\circ}$. SF10v400 – with a mean stellar age of $\sim 250 \text{ Myr}$ – forms stars earlier with respect to the other nearly face-on runs, while the difference between SF90v400 and the corresponding low velocity run SF90 is about 5 Myr at the leading edge and not significant in the rest of the external disk.

For the same runs we also plotted the final radial gas density profile (Fig. 18). In most of the cases a secondary peak is still present.

5 CONCLUSIONS

We have performed high resolution “wind tunnel” simulations to study the effects of ram-pressure by a tenuous Galactic hot halo on the HI morphology of the LMC's disk, its recent star formation history, and location of the youngest star

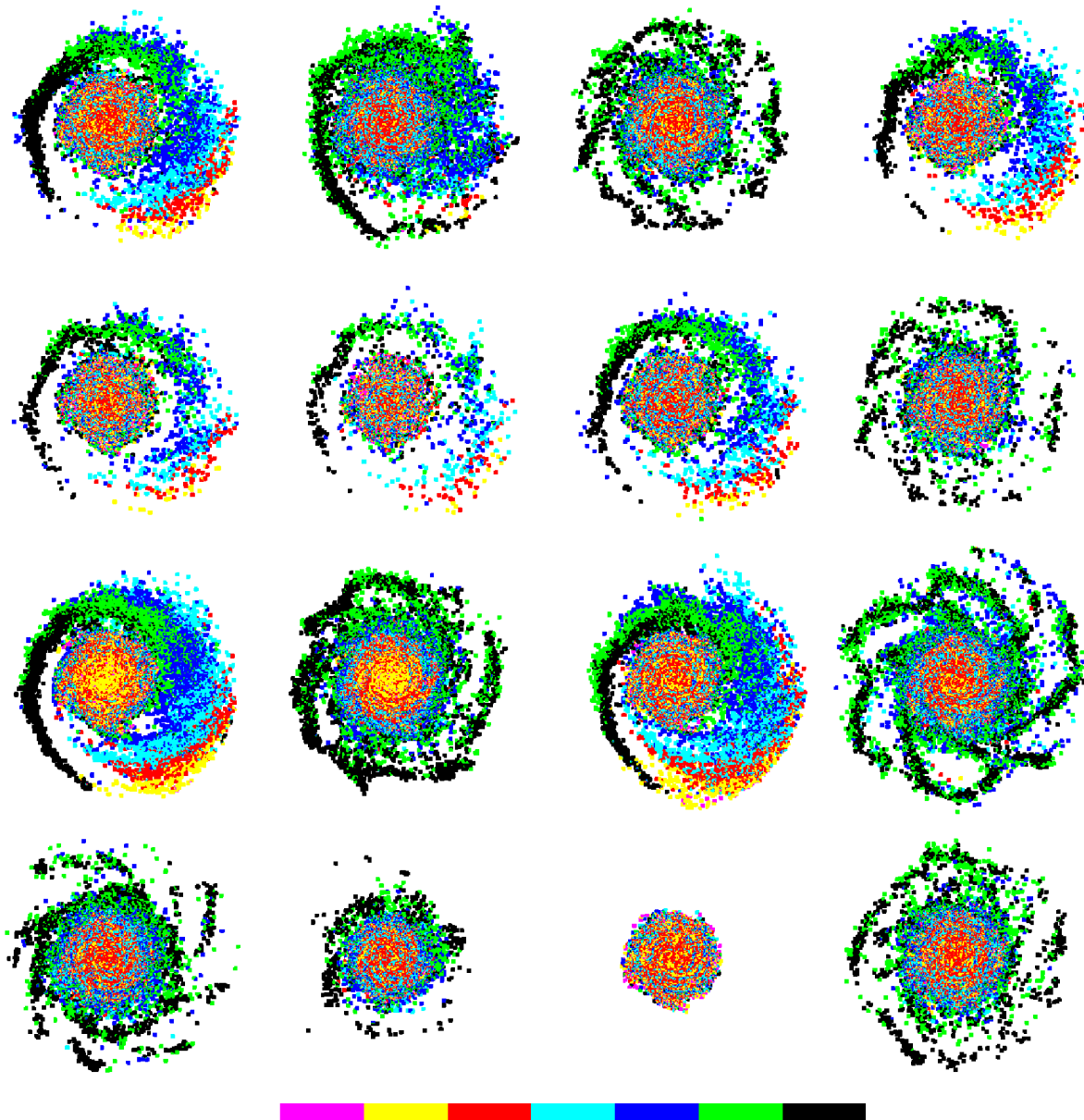


Figure 16. Age distribution of the newly forming stars in the LMC’s disk. The different panels represent (from top to bottom and from left to right) runs listed in Table 1: : SF90, SF45, SF10, SFconv, SFc1, SFconvc1, SF90c0.01, SF10c0.01, SF90c0.05, SF10c0.05, SF90v400, SF10v400, SF10v400t12000, SF10v400t15000, SFld90, SFld10. Magenta indicates stars older than 725 Myr.

forming regions. We did not focus on the mass loss produced by ram-pressure stripping since this would also be affected by tidal interactions. For the same reason our galaxies do not form any bar and we actually start with a galaxy model very stable against bar formation so that the pure effects of external pressure are more clearly visible. Our LMC is a multi-component system with a spherical NFW halo, an exponential stellar disk and a gaseous disk that extends up to 8 times the stellar disk scale length. In each simulation the external flux of hot particles increases with time as the satellite approaches the perigalacticon in such a way that the pressure experienced by the disk is consistent with the LMC’s orbital velocity and an average hot halo density of $2 \times 10^{-5} \text{ cm}^{-3}$ within 150 kpc from the Galactic center. Low velocity

runs are characterized by a “classic” pericentric velocity of 300 km s^{-1} (Mastropietro et al. 2005) while high velocity runs have velocities compatible with the new proper motion measurements of Kallivayalil et al. (2006). We expect the angle between the LMC’s disk and its proper motion to vary significantly during the last billion years of orbital interaction. We have defined the inclination angle i as the angle between the angular momentum vector of the disk and the flux of hot particles in the wind tube, so that the observed LMC’s disk would have $i \sim 60^\circ$. Mastropietro (2008) performed self consistent Nbody/SPH simulations of the interacting system MW/LMC adopting orbital constraints from the last LMC’s proper motion measurements and found that the Cloud enters the MW halo face-on ($i \sim 0^\circ$), moving nearly face-on for

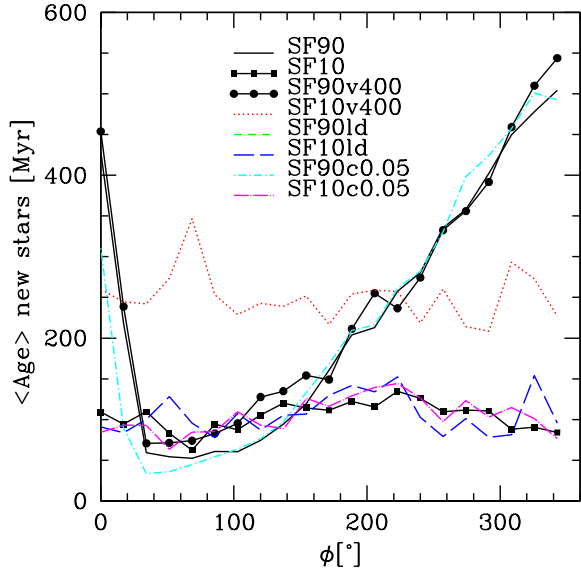


Figure 17. External disk mean stellar age in function of the azimuthal angle ϕ for selected runs in Table 1.

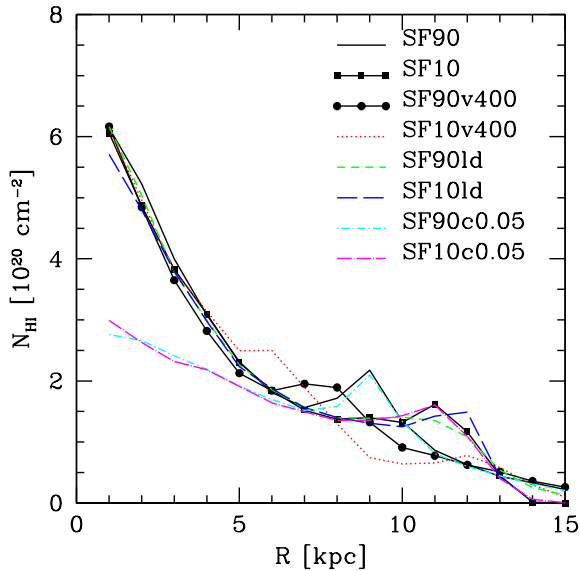


Figure 18. Azimuthally averaged HI column density profile of the final LMC disk for a selection of the runs listed in Fig. 1.

most of the last billion years. It turns edge-on only about 30 Myr ago. This means that the LMC is moving nearly edge-on close to the perigalactic passage, corresponding to the maximum ram-pressure values, consistently with the actual disk inclination measured by Kallivayalil et al. (2006).

We have performed several simulations varying the inclination angle of the disk, the star formation recipe and the intensity of the external pressure. We have shown that:

- The compression of the leading border of an edge-on LMC disk can account for the high density HI region observed at the south east. In our simulations this high density feature is well defined (with a mean density one order of

magnitude higher than the surrounding gas) and localized within 1.5 kpc from the border of the disk. Its average thickness and velocity dispersion along the line of sight are larger than the average values in the rest of the disk. In cool90 it extends for almost 160° and could also explain the origin of the spiral arm E described by Staveley-Smith et al. (2003), which does not have an equivalent in the stellar disk.

- Compression directed perpendicularly to the disk (in runs with $i < 90^\circ$) produces local instabilities in the gas distribution and a clumpy structure characterized by voids and high density filaments similar to those observed by the Parkes multibeam HI survey (see Fig. 3 of Staveley-Smith et al. 2003). If the satellite was moving nearly face-on in the past – and according to Mastropietro (2008) this is likely to happened during most of the LMC/MW orbital history – ram-pressure could be responsible for the general mottled appearance of the HI disk.

- As a result of the increase in density along the edge of the disk the mean HI column density shows a secondary peak at large radius, in agreement with observations.

- The compression of the satellite's IGM is naturally associated with induced star formation activity. We focussed on the external regions of the disk since the central parts of the real LMC would be dominated by the bar. Edge-on disks start forming stars earlier, but for large ram-pressure values the star formation rate of runs with $i < 90^\circ$ grows much faster. The high velocity edge-on model SF90v400 is characterized by a steeper increment in star formation at earlier times but later on the curve flattens and the star formation rate at the perigalacticon is similar to that of the low velocity case SF90. On the other hand, the star formation generated by a compression perpendicular to the LMC's disk increases with increasing ram-pressure values and in the case of the high velocity run SF10v400 reaches a peak ~ 1.5 times higher than in SF10. If the satellite is moving almost face-on until it gets very close to the perigalacticon we would expect not to see star formation before 0.6 Gyr independently of the orbital velocity. Differences between high and low velocity runs should be marginal also near the pericenter since star formation in edge-on runs – assuming our standard prescriptions – seems to saturate around $\sim 4 \times 10^4 M_\odot \text{ Myr}^{-1}$.

- In edge-on models the star formation of the external disk is characterized by a thin stellar arc along the leading border, well distinct from the star formation events in the central disk. If SFR is converted in $H\alpha$ luminosities, this arc breaks in several distinct and very luminous $H\alpha$ regions that more closely resemble the star forming complexes observed on the eastern border of the disk. Although the $H\alpha$ emission is mostly concentrated on the eastern side as a consequence of the very recent edge-on motion, we expect to see some luminous clumps forming a patchy distribution on the entire disk, due to gravitational instabilities and subsequent star formation induced by a nearly face-on compression of the disk before 30 Myr ago. As observed by de Boer et al. (1998) stellar complexes on the leading edge show a progression in age in the clockwise direction, but a face-on compression in the recent past of the LMC would circumscribe this trend to the youngest stellar regions, with age < 30 -40 Myr.

6 ACKNOWLEDGEMENTS

We would like to thank M-R. Cioni, T. Kaufmann and N. Kallivayalil for useful discussions. The numerical simulations were performed on the zBox1 supercomputer at the University of Zurich and on the local SGI-Altix 3700 Bx2 (partly funded by the cluster of excellence “Origin and Structure of the Universe”). This work was partly supported by the DFG Sonderforschungsbereich 375 “Astro-Teilchenphysik”.

REFERENCES

- Balsara, D. S. 1995, *J. Computational Physics*, 121, 2, 357-372
- Barnes, J. E. 2002, *MNRAS*, 333, 481
- Bekki, K., Chiba, M. 2005, *MNRAS*, 356, 680
- Besla, G., Kallivayalil, N., Hernquist, L., Robertson, B., Cox, T. J., van der Marel, R. P., & Alcock, C. 2007, *ApJ*, 668, 949
- Blumenthal, G. R., Faber, S. M., Flores, R., Primack, J. R. 1986, *ApJ*, 301, 27
- Blondiau, M. J., Kerp, J., Mebold, U., Klein, U. 1997, *A&A*, 323, 585
- Braun, J. M., Bomans, D. J., Will, J.-M., de Boer, K. S. 1997, *A&A*, 328, 167
- Broeils, A. H., van Woerden, H. 1994, *A&AS*, 107, 129
- Brüns, C., et al. 2005, *A&A*, 432, 45
- Cioni, M.-R. L., Girardi, L., Marigo, P., Habing, H. J. 2006, *A&A*, 448, 77
- Courteau, S. 1997, *AJ*, 114, 2402
- de Boer, K. S., Braun, J. M., Vallenari, A., Mebold, U. 1998, *A&A*, 329, L49
- de Marchi, G., Nota, A., Leitherer, C., Ragazzoni, R., Barbieri, C. 1993, *ApJ*, 419, 658
- Domainko, W., et al. 2006, *A&A*, 452, 795
- Evrard, A. E. 1988, *MNRAS*, 235, 911
- Fang, T., Mckee, C. F., Canizares, C. R., Wolfire, M. 2006, *ApJ*, 644, 174
- Gardiner, L. T., Sawa, T., Fujimoto, M. 1994, *MNRAS*, 266, 567
- Gardiner L. T., Noguchi M. 1996, *MNRAS*, 278, 191
- Gardner, J. P. 2001, *ApJ*, 557, 616
- Gerola, H., Seiden, P. E. 1978, *ApJ*, 223, 129
- Grebel, E. K., Brandner, W. 1998, *The Magellanic Clouds and Other Dwarf Galaxies*, Proceedings of the Bonn/Bochum-Graduiertenkolleg Workshop, 1998, p. 151
- Hernquist, L. 1993, *ApJ*, 86, 389
- Hunter, D. A., & Gallagher, J. S., III 1985, *AJ*, 90, 1789
- Jog, C. J., Solomon, P. M. 1984, *ApJ*, 276, 114
- Kallivayalil, N., van der Marel, R. P., Alcock, C., Axelrod, T., Cook, K. H., Drake, A. J., Geha, M. 2006, *ApJ*, 638, 772
- Katz, N. 1992, *ApJ*, 391, 502
- Katz, N., Weinberg, D. H., Hernquist, L. 1996, *ApJS*, 105, 19
- Kaufmann, T., Mayer, L., Wadsley, J., Stadel, J., Moore, B., *astroph* 0601115
- Kaufmann, T., Bullock, J. S., Maller, A. H., Fang, T., Wadsley, J. 2009, *arXiv:0812.2025*
- Kennicutt, R. C., Jr. 1989, *ApJ*, 344, 685
- Kennicutt, R. C., Jr. 1998, *ApJ*, 498, 541
- Kim S., Staveley-Smith L., Dopita M. A., Freeman K. C., Sault R. J., Kesteven M. J., McConnell D. 1998, *ApJ*, 503, 674
- Kronberger, T., Kapferer, W., Ferrari, C., Unterguggenberger, S., Schindler, S. 2008, *A&A*, 481, 337
- Livanou, E., Kontizas, M., Gonidakis, I., Kontizas, E., Maragoudaki, F., Oliver, S., Efstathiou, A., Klein, U. 2006, *A&A*, 451, 431
- Maller, A. H., Bullock, J. S. 2004, *MNRAS*, 355, 694
- Mastropietro, C., Moore, B., Mayer, L., Wadsley, J., Stadel, J. 2005, *MNRAS*, 363, 509 (M05)
- Mastropietro, C. 2008, *arXiv:0810.4155*
- Monaghan, J. J., Lattanzio, J. C. 1985, *A&A*, 149, 135
- Monaghan, J. J. 1992, *ARA&A*, 30, 543
- Navarro J. F., Frenk C. S., White S. D. M. 1997, *ApJ*, 490, 493
- Olsen, K. A. G., Salyk, C. 2002, *AJ*, 124, 2045
- Pedersen, K., Rasmussen, J., Sommer-Larsen, J., Toft, S., Benson, A. J., Bower, R. G. 2006, *New Astronomy*, 11, 465
- Persic, M., Salucci, P. 1997, *ASP Conf. Ser.* 117: Dark and Visible Matter in Galaxies and Cosmological Implications
- Piatek, S., Pryor, C., Olszewski, E. W. 2007, *ArXiv e-prints*, 712, *arXiv:0712.1764*
- Putman, M. E., Staveley-Smith, L., Freeman, K. C., Gibson, B. K., Barnes, D. G. 2003, *ApJ*, 586, 170
- Rafikov, R. R. 2001, *MNRAS*, 323, 445
- Rasmussen, J., Ponman, T. J., Mulchaey, J. S. 2006, *MNRAS*, 370, 453
- Roediger, E., Brüggén, M. 2006, *MNRAS*, 369, 567
- Sandage, A. 1986, *A&A*, 161, 89
- Silk, J., in *IAU Symp.* 115, *Star Forming Regions*, ed. M. Peimbert & J. Jugaku (Dordrecht:Reidel), 115, 663
- Springel, V., White, S. D. M. 1999, *MNRAS*, 307, 162
- Stadel, J. 2001, *Ph.D. Thesis*
- Staveley-Smith, L., Kim, S., Calabretta, M. R., Haynes, R. F., Kesteven, M. J. 2003, *MNRAS*, 339, 87
- Summers, F. J. 1993, *Ph.D. Thesis*,
- Toomre, A. 1964, *ApJ*, 139, 1217
- van der Marel, R. P. 2001, *AJ*, 122, 1827
- van der Marel, R. P., Cioni, M. L. 2001, *AJ*, 122, 1807
- van der Marel R. P., Alves D. R., Hardy E., Suntzeff N. B. 2002, *AJ*, 124, 2639
- Vollmer, B., Braine, J., Pappalardo, C., Hily-Blant, P. 2008, *A&A*, 491, 455
- Wadsley, J. W., Stadel, J., Quinn, T. 2004, *New Astronomy*, 9, 137
- Weinberg, M. D. 2000, *ApJ*, 532, 922
- Williams, R.J., et al. 2005, *ApJ*, 631, 856